Dalton Transactions

PAPER

View Article Online
View Journal | View Issue

Cite this: *Dalton Trans.*, 2017, **46**, 6202

A multiconfigurational approach to the electronic structure of trichromium extended metal atom chains†

M. Spivak,[a] V. Arcisauskaite,[b] X. López,[a] J. E. McGrady[b] and C. de Graaf*[a,c]

Density functional theory, Complete Active Space Self-Consistent Field (CASSCF) and perturbation theory (CASPT2) methodologies have been used to explore the electronic structure of a series of trichromium Extended Metal Atom Chains (EMACS) with different capping ligands. The study is motivated by the very different structural properties of these systems observed in X-ray experiments: the CN^--capped example has a symmetric Cr_3 unit while for the NO_3^--capped analogue the same unit has two very different Cr–Cr bond lengths. Density functional theory fails to locate an unsymmetric minimum for any of the systems studied, although the surface corresponding to the asymmetric stretch is very flat. CASPT2, in contrast, does locate an unsymmetric minimum only for the NO_3^--capped system, although again the surface is very flat. We use the Generalized active space (GASSCF) technique and effective Hamiltonian theory to interrogate the multi-configurational wavefunctions of these systems, and show that the increase in the σ–σ* separation as the chain becomes unsymmetric plays a defining role in the stability of the ground state and its expansion in terms of configuration state functions.

Received 27th March 2017,
Accepted 14th April 2017

DOI: 10.1039/c7dt01096f

rsc.li/dalton

Introduction

The chemistry of multiple bonds between transition metal ions is now well established in the inorganic literature, more than 50 years on from Cotton's discussion of the bonding in $[Re_2Cl_8]^{2-}$.[1] The quadruple bond is known for a variety of elements from the middle of the transition series (primarily group VI) and over the last decade the chemistry of the *trans*-bent quintuple bonds of Cr and Mo has also been developed.[1] The qualitative formulation of these bonds in LCAO terms is relatively straightforward, but translating this into an accurate quantum mechanical model has proven challenging. The fact that the static correlation is important in these systems has long been appreciated, leading to contributions from many configurations in a Multi-configurational Self Consistent Field (MCSCF) ansatz,[2–4] and to facile symmetry breaking in the context of unrestricted Hartree–Fock or density functional approaches.[5–11] The difficulty in describing both static and dynamic correlation in a balanced manner in these multiply bonded systems means that bimetallic species (either Cr_2 or ligated analogues) have been adopted as early test systems in the development of successive generations of electronic structure methods.[12–22] Recent interest in the possible role of metal–metal bonds in molecular electronics has motivated a concerted synthetic effort to extend metal chains beyond the dimeric unit. The most prominent compounds in this context are the "Extended Metal Atom Chains (EMACs)", the archetype of which is the trimetallic $M_3(dpa)_4X_2$ motif (Fig. 1, dpa = dipyridylamide).[23] This rapidly expanding family of compounds now includes homo- and heterometallic chains with lengths up 11 metals from all three transition series and a variety of terminal ligands, X. The latter can be used to tune the electronic properties of the chain, and, in the case of the cyanide and thiocyanate ligands, CN^- and NCS^-, attach the complex to metallic electrodes. Measurements of the electrical conductivity through the EMACs show a strong dependence on the identity of the metal,[22,24–32] suggesting that metal–metal bonding may play an important role in controlling electron transport.

From a theoretical perspective, the description of the chromium-containing members of the EMAC family such as $Cr_3(dpa)_4X_2$ is particularly challenging due to the presence of weak multiple bonding and hence substantial static correlation. The problem is compounded by the complex structural chemistry of this sub-class of EMACs, where the symmetry of the Cr_3 unit appears to be strongly dependent on the identity

[a]Departament de Quimica Fisica i Inorgànica, Universitat Rovira i Virgili, Marcellí Domingo s/n, E-43007 Tarragona, Spain. E-mail: coen.degraaf@urv.cat
[b]Department of Chemistry, Inorganic Chemistry Laboratory, University of Oxford, South Parks Road, Oxford OX1 3QR, UK
[c]ICREA, Passeig Lluis Companys 23, 08010 Barcelona, Spain

†Electronic supplementary information (ESI) available. See DOI: 10.1039/c7dt01096f

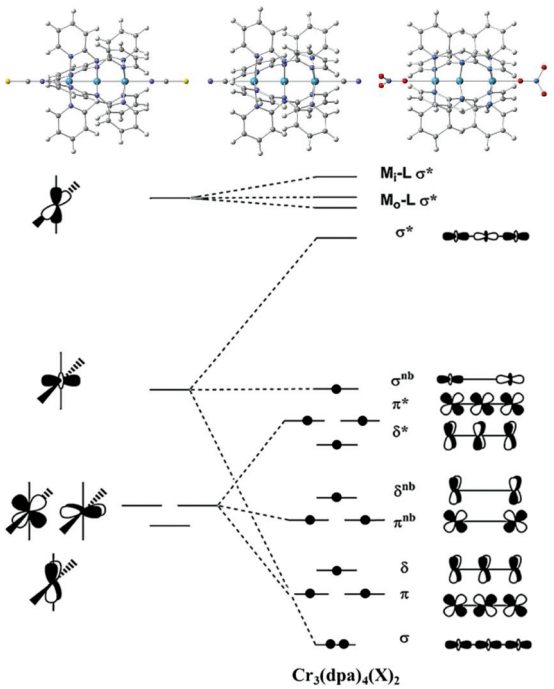

Fig. 1 Structures of the EMACs $Cr_3(dpa)_4(X)_2$, X = NCS^- (left), CN^- (center) and NO_3^- (right) and a schematic MO diagram. The atoms are colored in white (H), grey (C), blue (N), red (O), yellow (S) and light-blue (Cr).

of the terminal ligand. The consensus in the X-ray literature appears to be that truly symmetric Cr_3 chains are restricted to a small number of systems with very strong σ-donor ligands (CN^-, CCR^-). Otherwise an asymmetric structure is preferred, the most extreme examples being with very poor donors such as NO_3^- and BF_4^-.[24–27] Recent reports of heterometallic Cr_2M EMACs (M = Mn, Fe, Co, Ni, Zn) from the laboratories of Berry[28–32] and Nuss[33] confirm that highly asymmetric structures containing a quadruply bonded Cr_2 unit weakly coupled to a third metal centre, are ubiquitous. This suggests that the symmetric structures of $Cr_3(dpa)_4(CN)_2$ and $Cr_3(dpa)_4(CCR)_2$ are the exception rather than the rule. It is important at this point to also acknowledge a potentially defining role for the crystalline environment and/or temperature, neither of which are incorporated in simple computational models. The related tricobalt chains, $Co_3(dpa)_4X_2$, show extreme variations in structure, from symmetric to grossly unsymmetric, as a result of seemingly innocent changes in solvent of crystallization and/or temperature.[33–37] The concept of structure correlation pioneered by Bürgi and Dunitz[38] suggests that such variations in crystal structure map out relatively flat regions of the potential energy surface, because only then can the perturbations due to solvent/temperature exert a substantial influence on geometry. A computational analysis has confirmed that the surface for $Co_3(dpa)_4Cl_2$ is indeed flat, and that the low-lying regions map on to the experimental variations in crystal structure.[39] The body of structural data available for the Cr_3 EMACS is less extensive than that for the cobalt analogues, but a significant dependence on both solvent and temperature is apparent (Table 1). For example, crystallographic data measured at 296 K indicate that $Cr_3(dpa)_4(NCS)_2$ is unsymmetric, with Cr–Cr distances of 2.23 and 2.48 Å for a benzene solvate, but 2.21 and 2.46 Å for the corresponding toluene solvate.[25] Meanwhile, Surface Enhanced Raman Spectroscopy (SERS) experiments on $Cr_3(dpa)_4(NCS)_2$ adsorbed on silver nanoparticles in aqueous solution at temperatures up to 333.15 K are consistent with a symmetric structure.[26] Temperature also plays an important role in determining the structure of the

Table 1 Selected distances (Å) from the X-ray crystallography and from DFT and CASPT2

	Solvent	T (K)	$d(Cr_1–Cr_2)$	$d(Cr_2–Cr_3)$	$d(Cr_1–N)$ (av.)	$d(Cr_2–N)$ (av.)	$d(Cr_3–N)$ (av.)	$d(Cr_1–X)$	$d(Cr_3–X)$
$Cr_3(dpa)_4(CN)_2$									
X-Ray[25]	CH_2Cl_2	296	2.370	2.370	2.119	2.032	2.119	2.284	2.284
DFT			2.370	2.370	2.119	2.038	2.119	2.186	2.186
CASPT2			2.420	2.420	2.140	2.057	2.140	2.278	2.278
$Cr_3(dpa)_4(NCS)_2$									
X-Ray[25]	Benzene	296	2.234	2.482	2.114	2.037	2.114	2.203	2.203
X-Ray[25]	Toluene	296	2.215	2.465	2.116	2.020	2.116	2.203	2.203
DFT			2.369	2.369	2.116	2.039	2.116	2.105	2.105
CASPT2			2.330	2.330	2.133	2.063	2.133	2.233	2.233
$Cr_3(dpa)_4(NO_3)_2$									
X-Ray[25]	Et_2O	296	1.935	2.645	2.115	2.035	2.110	2.074	2.298
DFT			2.330	2.330	2.107	2.039	2.107	2.140	2.140
CASPT2			1.950	2.640	2.037	2.061	2.112	2.441	2.250
$Cr_3(dpa)_4Cl_2$									
X-Ray[25]	Benzene	296	2.222	2.489	2.117	2.029	2.119	2.539	2.525
X-Ray[25]	Benzene	296	2.234	2.482	2.116	2.028	2.116	2.539	2.548
X-Ray[25]	Toluene	296	2.236	2.482	2.121	2.032	2.124	2.559	2.553
X-Ray[25]	CH_2Cl_2	296	2.254	2.478	2.114	2.027	2.114	2.550	2.550
X-Ray[25]	Et_2O	296	2.248	2.469	2.110	2.031	2.120	2.508	2.552
X-Ray[40]	[a]	100	2.348	2.377	2.123	2.034	2.115	2.548	2.507
X-Ray[40]	[a]	15	2.367	2.369	2.120	2.032	2.111	2.534	2.495

[a] $(C_2H_5OC_2H_5)_x(CH_2Cl_2)_{1-x}$.

Cl^--capped analogue, $Cr_3(dpa)_4Cl_2$: the structure is distinctly unsymmetric at 296 K, irrespective of the solvent of crystallisation, but the difference between the Cr–Cr distances decreases at lower temperatures and at 15 K the molecule is almost perfectly symmetric.[25,40] In this case, room temperature SERS experiments are consistent with a symmetric structure but at 333.15 K the unsymmetric isomer appears in significantly greater concentrations.[26] This striking temperature and solvent dependence means that we must be cautious when comparing the results of computation (0 K, isolated molecule) to any single experimental data point.

In recent papers we have used broken-symmetry DFT to explore the factors that underpin the transition from symmetric to unsymmetric isomers of the Cr_3 chain in the EMACs, and the extent to which it affects their ability to conduct current.[34–37] We have argued that the conductivity is dominated by the orbitals of σ symmetry, primarily because these are the ones that remain substantially delocalized over both ends of the chain even under applied bias. Nevertheless, it is important to recognize that these systems present a very substantial challenge to density functional theory, and none of the commonly used functionals has proven able to reproduce the asymmetric structures found for $Cr_3(dpa)_4(NO_3)_2$. We emphasise again the caveat that comparison of the computed structure to any single X-ray experiment is difficult when the structure is known to be temperature- and solvent-dependent, but nevertheless the emergence of more unsymmetric structures with weaker donor ligands appears not to be captured by the computational model. One possible reason for this apparent failure is the extreme difficulty of providing a balanced description of static and dynamic correlation within the broken-symmetry ansatz. Motivated by this possibility, we now turn to multi-configurational methods (CASSCF/CASPT2) as an alternative tool to explore the structural chemistry of the $Cr_3(dpa)_4X_2$ family. Specifically, we focus on three members of the $Cr_3(dpa)_4X_2$ family with X = CN^-, NCS^- and NO_3^- which span the continuum between completely symmetric (CN^-) and highly unsymmetric (NO_3^-) limits.[25] This triad then provides a sensitive test of the ability of the CASPT2 methodology to capture subtle changes in static and dynamic correlation across a series of closely related molecules.

Computational methodology

Our approach in this paper is to consider the shape of two-dimensional potential energy surfaces for each of the three $Cr_3(dpa)_4X_2$ molecules, X = NO_3^-, NCS^- and CN^-, with the two Cr–Cr separations defining the independent variables. Given that geometry optimizations at the CASPT2 level are prohibitively expensive, we first map the surface using density functional theory, fixing the two independent Cr–Cr separations and allowing all other variables to optimize freely. These partially optimized structures are then taken as the basis for single point calculations at the CASPT2 level. DFT geometry optimizations were performed with GAUSSIAN 09,[41] using the BP86[42] functional and the def2-TZVP basis for Cr and def2-SVP for the other atoms (H, C, N, O, S).[43] The geometry is optimized for an $M_S = 2$ determinant with up–down–up spin ordering on the three Cr ions. Note that this determinant does not represent a pure quintet state but rather a mixture of different spin eigenfunctions, as is usual in the broken symmetry approach.[44] Multiconfigurational wave functions were constructed following the Complete Active Space Self-Consistent Field (CASSCF) approach using the MOLCAS 7.8 package.[45] The active space contains the twelve orbitals and twelve electrons shown in Fig. 2 (*i.e.* σ, σ^{nb}, σ*, doubly degenerate π, π^{nb}, π* and δ, δ^{nb} and δ*), with dynamic correlation included using Complete Active Space second-order Perturbation Theory (CASPT2)[46,47] with the CASSCF wavefunction as zeroth-order description.[48] Atomic natural orbitals optimized for relativistic corrections and core correlation (ANO–RCC) basis sets were used to expand the orbitals.[49] The large primitive set of functions is contracted to [2s] for H, [3s,2p] for C, [4s,3p,1d] for N and O, [4s,3p] for S and [6s,5p,4d,2f,1g] for Cr. Scalar relativistic effects were included using the Douglas–Kroll–Hess Hamiltonian. The computational costs from the two-electron integrals were reduced by the Cholesky decomposition technique (threshold was set to 10^{-8} Eh).[50] We used the standard zeroth-order Hamiltonian and an imaginary shift of 0.2 Eh to avoid the appearance of weak intruder states in the CASPT2 calculations. All single point calculations were performed for the electronic state with quintet multiplicity arising from the antiferromagnetic coupling of the local $S = 2$ spin moments of

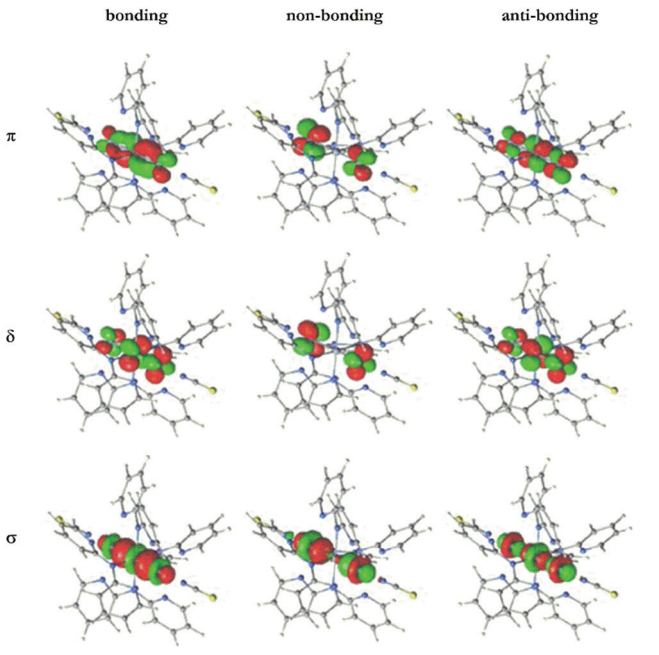

Fig. 2 Active molecular orbitals for $Cr_3(dpa)_4(NCS)_2$ of the CASSCF calculations. The MOs are classified in σ (bottom), δ (middle) and π (top) character and bonding (left), non-bonding (center) and anti-bonding (right) type. Only 3 out of 6 π orbitals are shown, the other three are obtained by a 90-degree rotation around the Cr–Cr–Cr axis.

the Cr(II) ions in the EMAC. The contour plots reported in this paper were obtained with the program Surfer® 12 (Golden Software, LLC). The Kriging interpolation method (slope = 1, anisotropy = 1; 0) was used to construct the surfaces from the calculated energies, which are represented as red dots.

Potential energy surfaces

Density functional theory

The potential energy surfaces of the ^{5}A ground states of $Cr_3(dpa)_4(CN)_2$, $Cr_3(dpa)_4(NCS)_2$, and $Cr_3(dpa)_4(NO_3)_2$ computed at the BP86 level of theory are compared in the left-hand column of Fig. 3, and the optimized parameters at the global minima are collected in Table 1. In all three cases, the global minimum corresponds to a totally symmetric structure lying along the lead diagonal, with a Cr–Cr separation of 2.37 Å for both CN^- and NCS^-, and 2.33 Å for the weaker donor NO_3^-. In Fig. 3, the lead diagonal corresponds to the symmetric stretching mode of the Cr_3 unit ($d(Cr_1–Cr_2) = d(Cr_2–Cr_3)$), and the global minimum is well defined in this direction. In contrast, the asymmetric stretching mode which links the top left and bottom right corners maps out a very flat valley, with less than 2 kcal mol^{-1} separating the global minimum from the highest point in any case. The shape of surface along the asymmetric stretching mode does, however, show some weak dependence on the identity of terminal ligand: the very flat valley extends further out on either side of the diagonal for NCS^- than for CN^-, and in the case of NO_3^- the extreme upper left and bottom right regions correspond to plateaus. In short, the gross features of the potential energy surfaces are consistent with experiment in so much as unsymmetric geometries are relatively favourable for NO_3^-, but nevertheless we are unable to locate a minimum, local or global, away from the lead diagonal. This reinforces the conclusion reached in our previous papers[37,51] that DFT systematically over-stabilizes the symmetric limit relative to the unsymmetric case.

CASSCF/CASPT2

In light of the well-known limitations of DFT in describing states with multiconfigurational character, we now turn to MCSCF methodologies for an alternative perspective on the metal–metal bonding. The active orbitals, depicted in Fig. 2, represent twelve different linear combinations of the atomic Cr-3d orbitals that hold the unpaired electrons of the Cr(II) ion in a (quasi-) octahedral coordination sphere (d_{xy}, d_{xz}, d_{yz}, d_{z^2}). The active orbitals are labeled as bonding, anti-bonding and non-bonding, and also by their symmetry character with respect to the rotation around the Cr–Cr–Cr axis: σ, π or δ.

The contour plots in Fig. 3 show that the CASPT2 potential energy surfaces for the ^{5}A ground states of $Cr_3(dpa)_4X_2$ are qualitatively similar to those obtained with DFT. The minima for X = CN^- and NCS^- again lie along the symmetric stretching coordinate, with a flat valley extending out along the asymmetric stretching mode. In the NO_3^--capped system $Cr_3(dpa)_4(NO_3)_2$, however, the differences between the two methodologies become most apparent. In this case a well-defined local minimum again appears along the lead diagonal ($d(Cr_1–Cr_2) = d(Cr_2–Cr_3) = 2.36$ Å), but two further minima appear at the extreme limits of the valley defined by the asymmetric stretching mode at $d(Cr_1–Cr_2) = 1.95$ Å, $d(Cr_2–Cr_3) = 2.64$ Å, in remarkable agreement with values of 1.93 Å and 2.64 Å from crystallography. On the BP86 surface these regions appeared as plateaus, 9 kcal mol^{-1} higher in energy than the symmetric global minimum but at the CASPT2 level the unsymmetric isomer is in fact the global minimum, albeit only by 0.7 kcal mol^{-1}. Thus, it seems that while the relative stabilization of the unsymmetric structures for the NO_3^--capped system *vs.* NCS^- and CN^- is apparent with both DFT and CASPT2, only the latter tips the balance such that they become the global minimum.

In the following section, we will analyse the CASSCF wavefunction in some detail, but before doing so it is important to establish whether the stabilization of the unsymmetric isomer is already apparent at the CASSCF level, or whether it emerges only as a result of the second order perturbation correction (CASPT2). The corresponding potential energy surfaces at the CASSCF level (ESI, Fig. S1†) are substantially different from the CASPT2 analogues shown in Fig. 3, confirming that the perturbation theory correction has a very significant impact on the energetics. On the CASSCF surfaces the symmetric minimum lies in a deep potential well, some 25–50 kcal mol^{-1} below the unsymmetric regions in the top left and bottom right corners: in other words, the PT2 correction stabilizes the unsymmetric regions relative to their symmetric analogues. Moreover, the magnitude of the PT2 correction is very dependent on the identity of the terminal ligand: for NCS^-, the relative stabilization of the unsymmetric isomer is almost 50 kcal mol^{-1} whereas for NO_3^- it is approximately half this amount. This very striking difference probably reflects the rather grey distinction between static and dynamic correlation in cases with many contributing configurations (*vide infra*). Nevertheless, it is clear that the CASSCF potential surfaces along the asymmetric stretching mode are very different in the CN^-, NCS^- and NO_3^- cases (indeed far more different than either the DFT or CASPT2 analogues), and so we now perform a detailed analysis of the CAS wave function in order to explore the origins of this effect.

Wave function analysis

The orbital array shown in Fig. 2 suggests a dominant $(\sigma)^2(\sigma^{nb})^1(\sigma^*)^0(\delta)^2(\delta^{nb})^1(\delta^*)^0\{(\pi)^2(\pi^{nb})^1(\pi^*)^0\}_{x,y}$ configuration, but the well-known multi-determinantal nature of wave functions for multiple bonds, particularly those containing first row metals, suggests that we should anticipate a more complex picture. The breakdown of the wavefunction for the symmetric isomer of $Cr_3(dpa)_4(NCS)_2$ shown in Table 2 (first column) indicates that there is, in fact, no single electronic configuration that dominates, and indeed the largest single contribution is only 11%. The situation becomes clearer if we con-

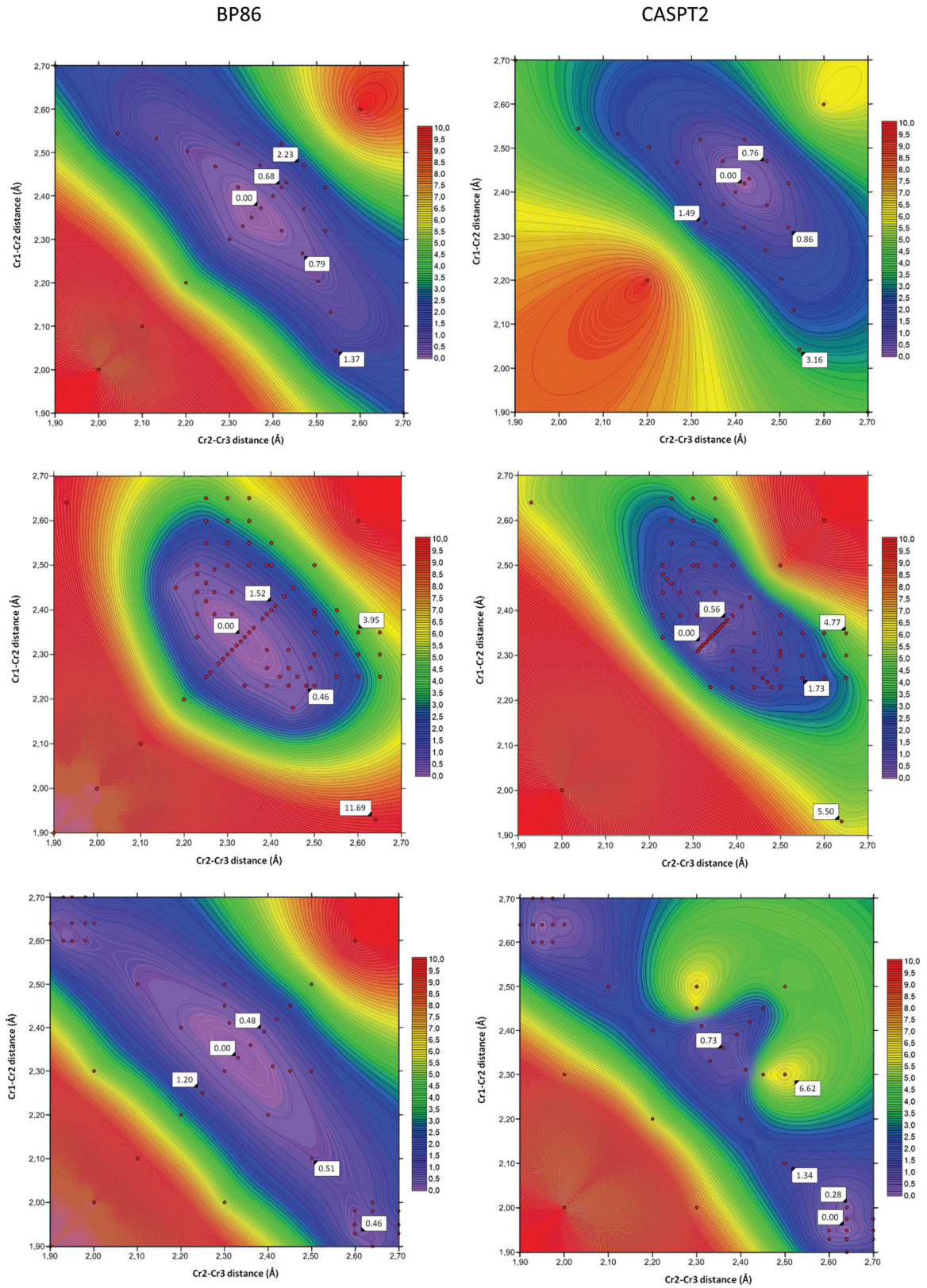

Fig. 3 Potential energy surfaces (kcal mol^{-1}) at the BP86 (left) and CASPT2 (right) levels of theory for $Cr_3(dpa)_4(CN)_2$ (top), $Cr_3(dpa)_4(NCS)_2$ (center) and $Cr_3(dpa)_4(NO_3)_2$ (bottom).

Table 2 Most important configurations (%) in the CAS(12,12) wavefunction for the symmetric (*d*(Cr–Cr) = 2.33 Å) and unsymmetric (*d*(Cr–Cr) = 1.93 Å and 2.64 Å) isomers of $Cr_3(dpa)_4(NCS)_2$. Relevant configurations arranged by the local σ manifold configuration

Configurations	Symmetric	Unsymmetric
$(\sigma)^2(\sigma_{nb})^1(\sigma^*)^0(\delta)^2(\delta_{nb})^1(\delta^*)^0(\pi)^2(\pi_{nb})^1(\pi^*)^0$	8.4	34.0
$(\sigma)^2(\sigma_{nb})^1(\sigma^*)^0(\delta)^2(\delta_{nb})^1(\delta^*)^0(\pi)^1(\pi_{nb})^1(\pi^*)^1$	7.3	2.5
$(\sigma)^2(\sigma_{nb})^1(\sigma^*)^0(\delta)^2(\delta_{nb})^1(\delta^*)^0(\pi)^0(\pi_{nb})^1(\pi^*)^2$	3.5	3.4
$(\sigma)^2(\sigma_{nb})^1(\sigma^*)^0(\delta)^1(\delta_{nb})^1(\delta^*)^1(\pi)^2(\pi_{nb})^1(\pi^*)^0$	10.9	6.7
$(\sigma)^2(\sigma_{nb})^1(\sigma^*)^0(\delta)^1(\delta_{nb})^1(\delta^*)^1(\pi)^1(\pi_{nb})^1(\pi^*)^1$	10.7	6.6
$(\sigma)^2(\sigma_{nb})^1(\sigma^*)^0(\delta)^1(\delta_{nb})^1(\delta^*)^1(\pi)^0(\pi_{nb})^1(\pi^*)^2$	4.7	0.9
$(\sigma)^2(\sigma_{nb})^1(\sigma^*)^0(\delta)^0(\delta_{nb})^1(\delta^*)^2(\pi)^2(\pi_{nb})^1(\pi^*)^0$	6.9	18.9
$(\sigma)^2(\sigma_{nb})^1(\sigma^*)^0(\delta)^0(\delta_{nb})^1(\delta^*)^2(\pi)^1(\pi_{nb})^1(\pi^*)^1$	6.1	1.7
$(\sigma)^2(\sigma_{nb})^1(\sigma^*)^0(\delta)^0(\delta_{nb})^1(\delta^*)^2(\pi)^0(\pi_{nb})^1(\pi^*)^2$	3.0	2.4
$(\sigma)^1(\sigma_{nb})^1(\sigma^*)^1(\delta)^2(\delta_{nb})^1(\delta^*)^0(\pi)^2(\pi_{nb})^1(\pi^*)^0$	3.2	1.9
$(\sigma)^1(\sigma_{nb})^1(\sigma^*)^1(\delta)^2(\delta_{nb})^1(\delta^*)^0(\pi)^1(\pi_{nb})^1(\pi^*)^1$	3.4	2.1
$(\sigma)^1(\sigma_{nb})^1(\sigma^*)^1(\delta)^2(\delta_{nb})^1(\delta^*)^0(\pi)^0(\pi_{nb})^1(\pi^*)^2$	1.6	0.5
$(\sigma)^1(\sigma_{nb})^1(\sigma^*)^1(\delta)^1(\delta_{nb})^1(\delta^*)^1(\pi)^2(\pi_{nb})^1(\pi^*)^0$	4.8	3.9
$(\sigma)^1(\sigma_{nb})^1(\sigma^*)^1(\delta)^1(\delta_{nb})^1(\delta^*)^1(\pi)^1(\pi_{nb})^1(\pi^*)^1$	5.3	1.2
$(\sigma)^1(\sigma_{nb})^1(\sigma^*)^1(\delta)^1(\delta_{nb})^1(\delta^*)^1(\pi)^0(\pi_{nb})^1(\pi^*)^2$	2.4	0.8
$(\sigma)^1(\sigma_{nb})^1(\sigma^*)^1(\delta)^0(\delta_{nb})^1(\delta^*)^2(\pi)^2(\pi_{nb})^1(\pi^*)^0$	2.7	1.3
$(\sigma)^1(\sigma_{nb})^1(\sigma^*)^1(\delta)^0(\delta_{nb})^1(\delta^*)^2(\pi)^1(\pi_{nb})^1(\pi^*)^1$	3.0	1.6
$(\sigma)^1(\sigma_{nb})^1(\sigma^*)^1(\delta)^0(\delta_{nb})^1(\delta^*)^2(\pi)^0(\pi_{nb})^1(\pi^*)^2$	1.4	0.4
$(\sigma)^0(\sigma_{nb})^1(\sigma^*)^2(\delta)^2(\delta_{nb})^1(\delta^*)^0(\pi)^2(\pi_{nb})^1(\pi^*)^0$	1.1	1.8
$(\sigma)^0(\sigma_{nb})^1(\sigma^*)^2(\delta)^2(\delta_{nb})^1(\delta^*)^0(\pi)^1(\pi_{nb})^1(\pi^*)^1$	1.2	0.4
$(\sigma)^0(\sigma_{nb})^1(\sigma^*)^2(\delta)^2(\delta_{nb})^1(\delta^*)^0(\pi)^0(\pi_{nb})^1(\pi^*)^2$	0.7	0.8
$(\sigma)^0(\sigma_{nb})^1(\sigma^*)^2(\delta)^1(\delta_{nb})^1(\delta^*)^1(\pi)^2(\pi_{nb})^1(\pi^*)^0$	1.6	0.6
$(\sigma)^0(\sigma_{nb})^1(\sigma^*)^2(\delta)^1(\delta_{nb})^1(\delta^*)^1(\pi)^1(\pi_{nb})^1(\pi^*)^1$	1.8	0.8
$(\sigma)^0(\sigma_{nb})^1(\sigma^*)^2(\delta)^1(\delta_{nb})^1(\delta^*)^1(\pi)^0(\pi_{nb})^1(\pi^*)^2$	1.0	0.3
$(\sigma)^0(\sigma_{nb})^1(\sigma^*)^2(\delta)^0(\delta_{nb})^1(\delta^*)^2(\pi)^2(\pi_{nb})^1(\pi^*)^0$	1.0	1.3
$(\sigma)^0(\sigma_{nb})^1(\sigma^*)^2(\delta)^0(\delta_{nb})^1(\delta^*)^2(\pi)^1(\pi_{nb})^1(\pi^*)^1$	1.1	0.3
$(\sigma)^0(\sigma_{nb})^1(\sigma^*)^2(\delta)^0(\delta_{nb})^1(\delta^*)^2(\pi)^0(\pi_{nb})^1(\pi^*)^2$	0.7	0.8

sider each symmetry-distinct manifold (σ, δ, π) in turn and collect together all configurations with a common component into so-called pseudo-configurations (PCs) (Table 3). For example, the combined weights of all the CSFs that contain $(\sigma)^2(\sigma^{nb})^1(\sigma^*)^0$, regardless of the distribution of electrons in the δ and π orbitals, make up 61.4% of the total wavefunction. The dominance of the $(\sigma)^2(\sigma^{nb})^1(\sigma^*)^0$ PC over its doubly excited counterpart, $(\sigma)^0(\sigma^{nb})^1(\sigma^*)^2$ (10.2%), would indicate a formal σ bond close to 1. At the opposite end of the spectrum, the near identical contributions of the $(\delta)^2(\delta^{nb})^1(\delta^*)^0$ and $(\delta)^0(\delta^{nb})^1(\delta^*)^2$ PCs (30.5% and 29.2%, respectively) are consistent with a negligible net contribution from δ bonding. The π manifold sits between these two extremes: contributions of 40.6% and 19.0% from $\{(\pi)^2(\pi^{nb})^1(\pi^*)^0\}_{x,y}$ and $\{(\pi)^0(\pi^{nb})^1(\pi^*)^2\}_{x,y}$, respectively, indicate a non-negligible contribution from π bonding, particularly given that there are two orthogonal π bonds to consider. The corresponding pseudo-configuration analysis for the unsymmetric isomer of $Cr_3(dpa)_4(NCS)_2$ (1.93–2.64 Å) in Table 3 shows that the multi-configurational character of the ground-state is reduced by the distortion, such that the $(\sigma)^2(\sigma_{nb})^1(\sigma^*)_0$ PC now contributes 77.5% of the wavefunction *vs.* 61.4% in the symmetric ground state. This enhanced contribution comes at the expense of the $(\sigma)^1(\sigma^{nb})^1(\sigma^*)^1$ PC whose contribution is reduced from 27.8% to 13.7%, suggesting that the distortion leads to a greater separation of the σ and σ* orbitals, and PCs where the latter is populated contribute correspondingly less to the ground-state wavefunction. Similar features are apparent in each of the symmetry-distinct manifolds, σ, δ and π, where the configurations with 2 electrons in the bonding orbital accumulate much larger weight compared to the symmetric case. Fig. 4 shows the σ natural molecular orbitals for symmetric (top) and asymmetric (bottom) isomers, from which it is apparent that the distortion has a strong localizing effect, with the bonding and antibonding orbitals accumulating on the short Cr_2 pair. The non-bonding orbital, in contrast, localizes almost entirely on the isolated Cr centre. The localization of the bonding/antibonding orbitals on a single diatomic unit has the effect of amplifying the bonding/antibonding character.

The effect of changing the terminal ligand (CN^-, NCS^-, NO_3^-) on the PCs weights is also summarised in Table 3: it is larger on the σ manifold than on the δ and π manifolds. The weight of σ configuration with 2 electrons in the bonding orbital ($(\sigma)^2(\sigma^{nb})^1(\sigma^*)^0$) increases marginally in the order NO_3^- < NCS^- < CN^- in both, symmetric and unsymmetric cases, indicating that the multi-configurational character of the wavefunction is maximised for the weakest σ-donor ligand (NO_3^-). Furthermore, the difference in weights between $(\sigma)^2(\sigma^{nb})^1(\sigma^*)^0$ and $(\sigma)^1(\sigma^{nb})^1(\sigma^*)^1$ configurations also increases in the order

Table 3 Dominant pseudo-configurations weights (%) for the three orbital manifolds in symmetric (*d*(Cr–Cr) = 2.33 Å) and unsymmetric (*d*(Cr–Cr) = 1.93 and 2.64 Å) isomers (structures of minimum energy) for the three compounds: $Cr_3(dpa)_4(CN)_2$, $Cr_3(dpa)_4(NCS)_2$ and $Cr_3(dpa)_4(NO_3)_2$

	Symmetric			Unsymmetric		
Pseudo-configurations	CN	NCS	NO_3	CN	NCS	NO_3
$(\sigma)^2(\sigma_{nb})^1(\sigma^*)^0$	62.1	61.4	60.9	77.8	77.5	76.7
$(\sigma)^1(\sigma_{nb})^1(\sigma^*)^1$	27.5	27.8	28.3	13.7	13.7	14.2
$(\sigma)^0(\sigma_{nb})^1(\sigma^*)^2$	10.0	10.2	10.4	7.0	7.0	7.6
$(\delta)^2(\delta_{nb})^1(\delta^*)^0$	30.6	30.5	30.7	48.1	48.0	47.8
$(\delta)^1(\delta_{nb})^1(\delta^*)^1$	43.2	43.1	43.3	22.0	22.0	22.6
$(\delta)^0(\delta_{nb})^1(\delta^*)^2$	26.0	26.0	25.9	29.3	29.2	28.9
$\{(\pi)^2(\pi_{nb})^1(\pi^*)^0\}_{x,y}$	40.8	40.6	40.7	71.4	71.2	70.5
$\{(\pi)^1(\pi_{nb})^1(\pi^*)^1\}_{x,y}$	39.9	39.9	40.0	17.5	17.6	18.0
$\{(\pi)^0(\pi_{nb})^1(\pi^*)^2\}_{x,y}$	18.9	19.0	19.0	10.5	10.5	10.9

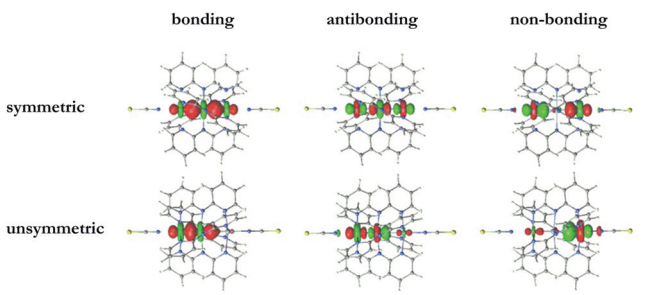

Fig. 4 Natural Molecular Orbitals of σ symmetry for the symmetric (top, 2.33–2.33 Å) and unsymmetric (bottom, 1.93–2.64 Å) $Cr_3(dpa)_4(NCS)_2$ structures. Orbitals are classified as bonding (left) antibonding (middle) and non-bonding (right).

NO_3^- < NCS^- < CN^-, suggesting that distortion leads to the largest separation of the σ and σ* orbitals in the $Cr_3(dpa)_4(CN)_2$ case. In what follows, we focus our attention on the σ manifold which is most sensitive to changes in the terminal ligand.

The absence of a single dominant configuration in the wavefunction makes it very difficult to analyse the factors that control the overall stabilization of the ground state and its tendency to distort. One way to overcome the problem of small CSF weights that has emerged in recent years is Effective Hamiltonian theory,[44,52,53] wherein the wavefunction is mapped onto a small model space spanned by a few conveniently chosen CSFs. The matrix elements of the Effective Hamiltonian (eqn (1)) obtained in this way condense all the information contained in the multi-configurational wavefunction into a few key matrix parameters, and in this case may provide a more transparent picture of the factors that govern the relative stability of symmetric and unsymmetric forms of Cr_3 chains. We construct a model space for the Effective Hamiltonian using eight CSFs of the general form $(\sigma)^A(\sigma^{nb})^B(\sigma^*)^C$ where A + B + C = 3. These eight CSFs correspond to (A, B, C) = (2, 1, 0), (1, 1, $\bar{1}$), (1, $\bar{1}$, 1), (0, 1, 2), (2, 0, 1), (1, 2, 0), (1, 0, 2) and (0, 2, 1), (0, 2, 1), and represent all symmetry-distinct ways of arranging three electrons in three orbitals with a net spin of 1/2 (the "bar" in (1, 1, $\bar{1}$) indicates opposite spin coupling to the other two electrons). To construct the Effective Hamiltonian matrix, eight CASSCF eigenvectors are needed with a large projection onto this model space. The elements (H_{ij}) of the Effective Hamiltonian matrix can be constructed using eqn (1) below, where CSF(k,i) are the orthonormalized projections onto model space of the ith configuration in the kth state (with energy $E(k)$).

$$H_{ij} = \sum_{k}^{\text{states}} \text{CSF}(k,i) \times E(k) \times \text{CSF}(k,j) \quad (1)$$

With the standard (12,12) active space used in the CASSCF calculations described above, the low-energy spectrum is dominated by excitations within the δ manifold, and amongst the lowest 100 roots we have been unable to locate any state with important contributions from configurations with two electrons in the σ^{nb} orbital. Since the description of the individual states is known to deteriorate with the number of roots in state-averaged CASSCF calculations, we chose not to seek even higher roots. Instead, we impose restrictions on the generation of the CSFs using the so-called General Active Space self-consistent field (GASSCF)[54,55] methodology. In the GASSCF approach, the active space can be subdivided into any number of orbital subspaces, each with a fixed number of electrons (minimum and maximum occupation). In this case, we divide the active space based on the symmetries of the orbitals (σ, δ, π_x and π_y) restricting the occupation of each subspace to minimize the number of CSFs. The σ subspace is forced to contain three electrons, in order to span all eight CSFs of the effective Hamiltonian alluded to above. For the δ and π manifolds, we define several single orbital subspaces in order to enforce CSFs with $(\delta)^1(\delta_{nb})^1(\delta^*)^1$ and $\{(\pi)^2(\pi_{nb})^1(\pi^*)^0\}_{x,y}$ arrangements (see Fig. S2 in ESI†), which are those with the largest contributions in the symmetric structure according to Table 3. The resulting configuration space is much smaller than the CASSCF one and amongst the lowest thirteen roots we were able to locate the eight states with the large projection onto the model space required to construct the Effective Hamiltonian matrix (see Tables S7–S18 in ESI†). The results are presented in Table 4(a) for the symmetric minimum structure of $Cr_3(dpa)_4(NCS)_2$. The eight CSFs spanned by the σ GAS can be separated on symmetry grounds into four *gerade* and four *ungerade* states, giving a block diagonal structure to the effective Hamiltonian matrix. Diagonalization of the upper 4 × 4 matrix spanned by the *ungerade* CSFs leads to a stabilization of the $(\sigma)^2(\sigma_{nb})^1(\sigma^*)^0$ configuration by 4.45 eV (Table 5, "stabilization"), with corresponding values of 4.34 eV for CN^- and 4.50 eV for NO_3^-. The lowest energy eigenvector of the effective Hamiltonian is also shown in Table 5 from which it is clear that the weights of the *ungerade* symmetry CSFs are very similar to those of the corresponding pseudo-configurations in the full CASSCF wavefunction shown in Table 3. The diagonal elements for the other three *ungerade* CSFs in the upper left quadrant of Table 4(a) are of similar magnitude, as are their off-diagonal elements with the $(\sigma)^2(\sigma_{nb})^1(\sigma^*)^0$ configuration, and as a result the other three configurations contribute with similar weight to the ground-state wavefunction. In summary, the restrictions imposed in the GASSCF process followed by projection onto a model space lead to a wavefunction that is qualitatively similar to the one that emerges from the full CASSCF calculation, but is much more easily interpreted.

In order to probe the origins of the unsymmetric structure of $Cr_3(dpa)_4(X)_2$, we have performed a parallel Effective Hamiltonian analysis on a marginally distorted structure which lies along the valley defined by the asymmetric stretching mode. ("u" in Table 4(b)). We have taken geometries where the Cr–Cr separations differ by 0.1 Å (2.28 Å and 2.38 Å), and allowed all other structural parameters to relax for each of $Cr_3(dpa)_4(NCS)_2$, $Cr_3(dpa)_4(CN)_2$ and $Cr_3(dpa)_4(NO_3)_2$ at the BP86 level of theory. The distortion is deliberately chosen to be small to facilitate comparison of the active orbitals with those in the symmetric form (that is, no substantial localization on the Cr_2 unit). The elimination of the inversion centre means that there is no longer a rigorous distinction between the *gerade* and *ungerade* CSFs, and off-diagonal elements as large as 1.5 eV appear between the two blocks as a result. However, this mixing between *gerade* and *ungerade* functions has negligible direct influence on the stabilization of the $(\sigma)^2(\sigma_{nb})^1(\sigma^*)^0$ CSF: the contribution of the *gerade* CSFs to the ground-state wavefunction is negligible, and indeed diagonalization of the 4 × 4 upper left quadrant of the matrix in Table 4(b) gives energies that are almost identical to those obtained from diagonalization of the full 8 × 8 matrix. Nevertheless, compared to the symmetric structure, the stabilization of the $(\sigma)^2(\sigma_{nb})^1(\sigma^*)^0$ CSF upon diagonalisation is somewhat smaller, 4.17 eV *vs.* 4.45 eV and the dominant configuration has a slightly higher weight, both of which confirm that the multi-configurational character

Table 4 Effective Hamiltonian matrices for (a) the symmetric $Cr_3(dpa)_4(NCS)_2$ minimum and (b) a marginally unsymmetric form. All elements are given in eV. Diagonal terms are shifted so A_{11} = 0 for comparison

(a) Symmetric (d(Cr–Cr) = 2.33 Å).

CSFs		1	2	3	4	5	6	7	8
1	$(\sigma)^2(\sigma_{nb})^1(\sigma^*)^0$	0.00	4.24	−3.43	4.60	0.00	0.00	0.00	0.00
2	$(\sigma)^u(\sigma_{nb})^u(\sigma^*)^d$	4.24	10.68	−0.19	−5.27	0.00	0.00	0.00	0.00
3	$(\sigma)^u(\sigma_{nb})^d(\sigma^*)^u$	−3.43	−0.19	11.50	1.60	0.00	0.00	0.00	0.00
4	$(\sigma)^0(\sigma_{nb})^1(\sigma^*)^2$	4.60	−5.27	1.60	13.64	0.00	0.00	0.00	0.00
5	$(\sigma)^2(\sigma_{nb})^0(\sigma^*)^1$	0.00	0.00	0.00	0.00	5.05	−4.29	1.42	4.24
6	$(\sigma)^1(\sigma_{nb})^2(\sigma^*)^0$	0.00	0.00	0.00	0.00	−4.29	5.87	4.66	2.91
7	$(\sigma)^1(\sigma_{nb})^0(\sigma^*)^2$	0.00	0.00	0.00	0.00	1.42	4.66	11.97	−4.29
8	$(\sigma)^0(\sigma_{nb})^2(\sigma^*)^1$	0.00	0.00	0.00	0.00	4.24	2.91	−4.29	12.54

(b) Marginally unsymmetric (d(Cr–Cr) = 2.28, 2.38 Å).

CSFs		1	2	3	4	5	6	7	8
1	$(\sigma)^2(\sigma_{nb})^1(\sigma^*)^0$	0.00	3.93	−3.37	4.61	−0.47	0.57	−0.55	0.51
2	$(\sigma)^u(\sigma_{nb})^u(\sigma^*)^d$	3.93	10.52	0.00	−5.12	−1.40	1.35	−1.04	1.11
3	$(\sigma)^u(\sigma_{nb})^d(\sigma^*)^u$	−3.37	0.00	11.65	1.29	0.64	−1.13	0.62	−0.64
4	$(\sigma)^0(\sigma_{nb})^1(\sigma^*)^2$	4.61	−5.12	1.29	14.14	0.51	−0.54	0.79	−0.90
5	$(\sigma)^2(\sigma_{nb})^0(\sigma^*)^1$	−0.47	−1.40	0.64	0.51	5.27	4.07	−1.15	4.00
6	$(\sigma)^1(\sigma_{nb})^2(\sigma^*)^0$	0.57	1.35	−1.13	−0.54	4.07	6.32	4.47	−2.85
7	$(\sigma)^1(\sigma_{nb})^0(\sigma^*)^2$	−0.55	−1.04	0.62	0.79	−1.15	4.47	12.44	4.06
8	$(\sigma)^0(\sigma_{nb})^2(\sigma^*)^1$	0.51	1.11	−0.64	−0.90	4.00	−2.85	4.06	13.28

Table 5 Stabilisation of the $(\sigma)^2(\sigma_{nb})^1(\sigma^*)^0$ CSF and contributions (%) of the different GAS CSFs to the ground-state GASSCF wave function for different symmetric (d(Cr–Cr) = 2.33 Å) and marginally unsymmetric (d(Cr–Cr) = 2.28 and 2.38 Å) structures

		Symmetric			Marginally unsymmetric		
		CN	NCS	NO_3	CN	NCS	NO_3
	Stabilisation/eV	4.34	4.45	4.50	4.09	4.17	4.31
1	$(\sigma)^2(\sigma_{nb})^1(\sigma^*)^0$	70.7	70.0	69.5	72.7	72.3	71.1
2	$(\sigma)^u(\sigma_{nb})^u(\sigma^*)^d$	4.4	4.5	4.5	4.0	4.0	4.2
3	$(\sigma)^u(\sigma_{nb})^d(\sigma^*)^u$	12.0	12.1	12.3	10.6	10.7	11.6
4	$(\sigma)^0(\sigma_{nb})^1(\sigma^*)^2$	10.9	11.2	11.4	10.5	10.7	10.9
5	$(\sigma)^2(\sigma_{nb})^0(\sigma^*)^1$	0.0	0.0	0.0	0.2	0.2	0.1
6	$(\sigma)^1(\sigma_{nb})^2(\sigma^*)^0$	0.0	0.0	0.0	0.2	0.2	0.1
7	$(\sigma)^1(\sigma_{nb})^0(\sigma^*)^2$	0.0	0.0	0.0	0.2	0.2	0.1
8	$(\sigma)^0(\sigma_{nb})^2(\sigma^*)^1$	0.0	0.0	0.0	0.2	0.2	0.1

is reduced by the low-symmetry distortion (note that the changes in weight are less dramatic than those shown for the pseudo-configurations in Table 3 because the degree of distortion is less). If we compare in detail the Effective Hamiltonian matrices in Table 4(a) and (b), the key difference that leads to the reduced stabilization of the ground state appears to be the off-diagonal H_{12} element between the $(\sigma)^2(\sigma_{nb})^1(\sigma^*)^0$ and $(\sigma)^1(\sigma_{nb})^1(\sigma^*)^1$ CSFs. From eqn (1), H_{12} is large only when the projections onto both configurations are large and comparable in the same state k (*i.e.* CSF(k, 1), CSF(k, 2) are both large), and this will occur when their energetic separation is small.

In the case of $Cr_3(dpa)_4(NCS)_2$, H_{12} drops from 4.24 eV to 3.93 eV which reflects the increased separation between the σ and σ* orbitals induced by the shortening of one Cr–Cr bond, precisely the same phenomenon that led to the reduced contribution of the $(\sigma)^1(\sigma_{nb})^1(\sigma^*)^1$ PC in Table 3 although again the changes in Table 3 are magnified by the much greater distortion in that case.

Finally, we can use the Effective Hamiltonian analysis to explore the origins of the terminal ligand effect in the series $Cr_3(dpa)_4(NO_3)_2$, $Cr_3(dpa)_4(NCS)_2$, $Cr_3(dpa)_4(CN)_2$ (Table 5). For the symmetric structures, the stabilization energies decrease and the contributions of the dominant configuration increase in the order $NO_3^- \rightarrow NCS^- \rightarrow CN^-$, indicating that the multi-configurational character of the wavefunction is maximized for the weakest σ-donor ligand. Moreover, the loss in correlation energy upon distortion is less in the NO_3^- case (4.50–4.31 = 0.19 eV) than it is in NCS^- (4.45–4.17 = 0.28 eV), indicating that the former is less affected by the distortion. This observation correlates with the relative stabilization of the unsymmetric limit noted for $Cr_3(dpa)_4(NO_3)_2$ in the CASSCF and CASPT2 potential energy surfaces. Moreover, all the changes in

stabilization energy correlate with changes in the magnitude of the H_{12} matrix element (the reduced multiconfigurational character results in smaller H_{12}, which in turn reduces the stabilization energies), establishing a clear causal link between the stabilization of the ground state through multi-configurational effects and the relative destabilization of the σ* orbital.

Conclusions

In this work, we have employed the CASSCF, GASSCF and CASPT2 methodologies to interrogate the electronic structure of a series of trichromium extended metal atom chains, $Cr_3(dpa)_4X_2$. The most striking feature of this class of compounds is its structural flexibility: examples are known where the Cr_3 unit is totally symmetric and other where it is grossly unsymmetric. The precise details of the structure are dependent on temperature and also on solvent of crystallization as well as the identity of the ligand X, but the limited data available suggests that there is a distinct shift towards more unsymmetric structures for weaker donor ligands such as NO_3^-. Density functional theory (here in the form of the BP86 functional) indicates that the potential energy surface describing the Cr–Cr–Cr asymmetric stretch is very flat in all cases, and that the highly distorted regions are somewhat stabilized relative to the symmetric structure for X = NO_3^- rather than X = CN^-. Nevertheless, DFT fails to reproduce an unsymmetric minimum on the gas-phase potential energy surface in any case, with the global minimum lying instead along the symmetric stretching coordinate.

At the CASPT2 level, in contrast, an unsymmetric global minimum does emerge in the case of NO_3^- but not for NCS^- or CN^-, although once again the asymmetric stretch is extremely flat with less than 1 kcal mol^{-1} separating symmetric and unsymmetric limits. This whilst the subtle differences in the computed surfaces are consistent with experiment, the dependence on terminal ligand is only very marginal. The CASSCF wavefunction is in all cases extremely multi-determinantal, with no single configuration state function contributing more than 11% in the symmetric limit and 34% in the unsymmetric form. We can, however, collect together all the CSFs that share a common feature, for example the same occupancy of orbitals with σ symmetry, into distinct 'pseudo-configurations'. It then becomes clear that the $(\sigma)^2(\sigma_{nb})^1(\sigma^*)^0$ pseudo-configuration, where the σ orbital is doubly occupied, dominates over those where it is either singly occupied or vacant. Moreover, multiconfigurational character is much less pronounced in the unsymmetric limit, which is reasonably well described by the single $(\sigma)^2(\sigma_{nb})^1(\sigma^*)^0$ pseudo-configuration (77.5% of the wavefunction), and for any given geometry of the Cr_3 unit, the wavefunction is marginally more multi-configurational for the NO_3^- ligand.

To obtain a more transparent picture, we have mapped the eight CSFs generated by excitations within the $\sigma/\sigma_{nb}/\sigma^*$ manifold onto an effective model Hamiltonian. The states of interest were generated using the GASSCF approach which allows us to constrain the excitations to the subset of orbitals with local σ symmetry. From this analysis, we conclude that the destabilization of the σ* orbital as the system is distorted away from the symmetric minimum reduces the extent to which the ground-state configuration is stabilized by excited configurations where this orbital is singly or doubly occupied. This stabilization is largest for the NO_3^- case because it is more multi-configurational, and the loss of correlation energy upon distortion is smallest. Whilst these effects are undeniably small, the characteristics of the matrix elements of the effective Hamiltonian do correlate directly with the greater tendency to distort in $Cr_3(dpa)_4(NO_3)_2$ which is apparent in both the CASPT2 surfaces and the experimental data.

Acknowledgements

Financial support has been provided by the Spanish Administration (CdG, Project CTQ2014-51938-P), the Generalitat de Catalunya (CdG, Projects 2014SGR199 and Xarxa d'R+D+I en Química Teòrica i Computacional, XRQTC) and the European Union (JEM, CdG, COST Action ECOST-Bio CM1305). We also thank the EPSRC for financial support (JEM, VA, EP/K021435/1).

References

1 F. A. Cotton, C. A. Murillo and R. A. Walton, *Multiple Bonds Between Metal Atoms*, Springer, US, 2005.
2 P. J. Hay, *J. Am. Chem. Soc.*, 1978, **100**, 2897–2898.
3 J.-P. Blaudeau, R. B. Ross, R. M. Pitzer, P. Mougenot and M. Benard, *J. Phys. Chem.*, 1994, **98**, 7123–7127.
4 K. Saito, Y. Nakao, H. Sato and S. Sakaki, *J. Phys. Chem. A*, 2006, **110**, 9710–9717.
5 L. Noodleman and J. G. Norman, Jr., *J. Chem. Phys.*, 1979, **70**, 4903–4906.
6 K. E. Edgecombe and A. D. Becke, *Chem. Phys. Lett.*, 1995, **244**, 427–432.
7 B. Delley, A. J. Freeman and D. E. Ellis, *Phys. Rev. Lett.*, 1983, **50**, 488–491.
8 N. A. Baykara, B. N. McMaster and D. R. Salahub, *Mol. Phys.*, 1984, **52**, 891–905.
9 J. E. McGrady, R. Stranger and T. Lovell, *J. Phys. Chem. A*, 1997, **101**, 6265–6272.
10 T. Lovell, J. E. McGrady, R. Stranger and S. A. Macgregor, *Inorg. Chem.*, 1996, **35**, 3079–3080.
11 J. E. McGrady, T. Lovell and R. Stranger, *Inorg. Chem.*, 1997, **36**, 3242–3247.
12 B. O. Roos, *Collect. Czech. Chem. Commun.*, 2003, **68**, 265.
13 N. E. Schultz, Y. Zhao and D. G. Truhlar, *J. Phys. Chem. A*, 2005, **109**, 4388–4403.
14 M. M. Goodgame and W. A. Goddard, *Phys. Rev. Lett.*, 1985, **54**, 661–664.
15 C. W. Bauschlicher and H. Partridge, *Chem. Phys. Lett.*, 1994, **231**, 277–282.

16 N. Desmarais, F. A. Reuse and S. N. Khanna, *J. Chem. Phys.*, 2000, **112**, 5576–5584.
17 L. Gagliardi and B. O. Roos, *Nature*, 2005, **433**, 848–851.
18 M. Brynda, L. Gagliardi, P.-O. Widmark, P. P. Power and B. O. Roos, *Angew. Chem., Int. Ed.*, 2006, **45**, 3804–3807.
19 C. R. Landis and F. Weinhold, *J. Am. Chem. Soc.*, 2006, **128**, 7335–7345.
20 G. Merino, K. J. Donald, J. S. D'Acchioli and R. Hoffmann, *J. Am. Chem. Soc.*, 2007, **129**, 15295–15302.
21 L.-C. Wu, C.-W. Hsu, Y.-C. Chuang, G.-H. Lee, Y.-C. Tsai and Y. Wang, *J. Phys. Chem. A*, 2011, **115**, 12602–12615.
22 D. W. Brogden, Y. Turov, M. Nippe, G. Li Manni, E. A. Hillard, R. Clérac, L. Gagliardi and J. F. Berry, *Inorg. Chem.*, 2014, **53**, 4777–4790.
23 S.-A. Hua, M.-C. Cheng, C.-h. Chen and S.-M. Peng, *Eur. J. Inorg. Chem.*, 2015, **2015**, 2510–2523.
24 R. Clérac, F. A. Cotton, L. M. Daniels, K. R. Dunbar, C. A. Murillo and I. Pascual, *Inorg. Chem.*, 2000, **39**, 748–751.
25 J. F. Berry, F. A. Cotton, T. Lu, C. A. Murillo, B. K. Roberts and X. Wang, *J. Am. Chem. Soc.*, 2004, **126**, 7082–7096.
26 C.-J. Hsiao, S.-H. Lai, I. C. Chen, W.-Z. Wang and S.-M. Peng, *J. Phys. Chem. A*, 2008, **112**, 13528–13534.
27 S.-Y. Lin, I. W. P. Chen, C.-h. Chen, M.-H. Hsieh, C.-Y. Yeh, T.-W. Lin, Y.-H. Chen and S.-M. Peng, *J. Phys. Chem. B*, 2004, **108**, 959–964.
28 M. Nippe and J. F. Berry, *J. Am. Chem. Soc.*, 2007, **129**, 12684–12685.
29 M. Nippe, Y. Turov and J. F. Berry, *Inorg. Chem.*, 2011, **50**, 10592–10599.
30 M. Nippe, E. Victor and J. F. Berry, *Eur. J. Inorg. Chem.*, 2008, **2008**, 5569–5572.
31 M. Nippe, J. Wang, E. Bill, H. Hope, N. S. Dalal and J. F. Berry, *J. Am. Chem. Soc.*, 2010, **132**, 14261–14272.
32 M. Nippe, E. Bill and J. F. Berry, *Inorg. Chem.*, 2011, **50**, 7650–7661.
33 D. Aydin-Cantürk and H. Nuss, *Z. Anorg. Allg. Chem.*, 2011, **637**, 543–546.
34 M.-M. Rohmer and M. Bénard, *J. Am. Chem. Soc.*, 1998, **120**, 9372–9373.
35 M.-M. Rohmer, A. Strich, M. Bénard and J.-P. Malrieu, *J. Am. Chem. Soc.*, 2001, **123**, 9126–9134.
36 M.-M. Rohmer and M. Benard, *Chem. Soc. Rev.*, 2001, **30**, 340–354.
37 V. P. Georgiev and J. E. McGrady, *J. Am. Chem. Soc.*, 2011, **133**, 12590–12599.
38 H.-B. Bürgi and J. D. Dunitz, *Structure Correlation*, Wiley, 2008.
39 D. A. Pantazis and J. E. McGrady, *J. Am. Chem. Soc.*, 2006, **128**, 4128–4135.
40 L. C. Wu, M. K. Thomsen, S. R. Madsen, M. Schmoekel, M. R. V. Jorgensen, M. C. Cheng, S. M. Peng, Y. S. Chen, J. Overgaard and B. B. Iversen, *Inorg. Chem.*, 2014, **53**, 12489–12498.
41 M. J. Frisch, G. W. Trucks, H. B. Schlegel, G. E. Scuseria, M. A. Robb, J. R. Cheeseman, G. Scalmani, V. Barone, B. Mennucci, G. A. Petersson, M. C. H. Nakatsuji, X. Li, H. P. Hratchian, A. F. Izmaylov, J. Bloino, G. Zheng, J. L. Sonnenberg, M. Hada, M. Ehara, K. Toyota, R. Fukuda, J. Hasegawa, M. Ishida, T. Nakajima, Y. Honda, O. Kitao, H. Nakai, T. Vreven, J. J. A. Montgomery, J. E. Peralta, F. Ogliaro, M. Bearpark, J. J. Heyd, E. Brothers, K. N. Kudin, V. N. Staroverov, R. K. T. Keith, J. Normand, K. Raghavachari, A. Rendell, J. C. Burant, S. S. Iyengar, J. Tomasi, M. Cossi, N. Rega, J. M. Millam, M. Klene, J. E. Knox, J. B. Cross, V. Bakken, C. Adamo, J. Jaramillo, R. Gomperts, E. Stratmann, O. Yazyev, A. J. Austin, R. Cammi, C. Pomelli, J. W. Ochterski, R. L. Martin, K. Morokuma, V. G. Zakrzewski, G. A. Voth, P. Salvador, J. J. Dannenberg, S. Dapprich, A. D. Daniels, O. Farkas, J. B. Foresman, J. V. Ortiz, J. Cioslowski and D. J. Fox, *Gaussian 09 Revision D.01*, Gaussian Inc.
42 A. D. Becke, *J. Chem. Phys.*, 1996, **104**, 1040–1046.
43 F. Weigend and R. Ahlrichs, *Phys. Chem. Chem. Phys.*, 2005, **7**, 3297–3305.
44 J. P. Malrieu, R. Caballol, C. J. Calzado, C. de Graaf and N. Guihéry, *Chem. Rev.*, 2014, **114**, 429–492.
45 F. Aquilante, J. Autschbach, R. K. Carlson, L. F. Chibotaru, M. G. Delcey, L. De Vico, I. Fernández-Galván, N. Ferré, L. M. Frutos, L. Gagliardi, M. Garavelli, A. Giussani, C. E. Hoyer, G. Li Manni, H. Lischka, D. Ma, P. Å. Malmqvist, T. Müller, A. Nenov, M. Olivucci, T. B. Pedersen, D. Peng, F. Plasser, B. Pritchard, M. Reiher, I. Rivalta, I. Schapiro, J. Segarra-Martí, M. Stenrup, D. G. Truhlar, L. Ungur, A. Valentini, S. Vancoillie, V. Veryazov, V. P. Vysotskiy, O. Weingart, F. Zapata and R. Lindh, *J. Comput. Chem.*, 2016, **37**, 506–541.
46 K. Andersson, P. A. Malmqvist, B. O. Roos, A. J. Sadlej and K. Wolinski, *J. Phys. Chem.*, 1990, **94**, 5483–5488.
47 K. Andersson, P. Å. Malmqvist and B. O. Roos, *J. Chem. Phys.*, 1992, **96**, 1218–1226.
48 P. G. Szalay, T. Müller, G. Gidofalvi, H. Lischka and R. Shepard, *Chem. Rev.*, 2012, **112**, 108–181.
49 B. O. Roos, V. Veryazov and P.-O. Widmark, *Theor. Chem. Acc.*, 2004, **111**, 345–351.
50 F. Aquilante, P.-Å. Malmqvist, T. B. Pedersen, A. Ghosh and B. O. Roos, *J. Chem. Theory Comput.*, 2008, **4**, 694–702.
51 V. Arcisauskaite, M. Spivak and J. E. McGrady, *Inorg. Chim. Acta*, 2015, **424**, 293–299.
52 C. Bloch, *Nucl. Phys.*, 1958, **6**, 329–347.
53 J. des Cloizeaux, *Nucl. Phys.*, 1960, **20**, 321–346.
54 T. Fleig, J. Olsen and L. Visscher, *J. Chem. Phys.*, 2003, **119**, 2963–2971.
55 D. Ma, G. L. Manni and L. Gagliardi, *J. Chem. Phys.*, 2011, **135**, 044128.